Chemical Science

ROYAL SOCIETY OF CHEMISTRY

EDGE ARTICLE

View Article Online
View Journal | View Issue

Cite this: *Chem. Sci.*, 2025, **16**, 13374

All publication charges for this article have been paid for by the Royal Society of Chemistry

Received 13th March 2025
Accepted 18th June 2025

DOI: 10.1039/d5sc01980j

rsc.li/chemical-science

Side-chain ionization enables ultrafast intramolecular singlet fission in the azaquinodimethane skeleton†

Zixiang Wu,[a] Christopher L. Anderson,[b] Teng-Shuo Zhang,*[c] Yi Liu,*[b] Hongbing Fu*[d] and Long Wang*[a]

Singlet fission (SF) could significantly alleviate thermalization losses of high-energy photons, thus holding great potential for improving the power conversion efficiency of solar cells. Conventional SF materials require an intricate control of molecular packing motifs in the solid state to achieve efficient multiexciton generation. Small molecule intramolecular singlet fission (iSF) materials have emerged as promising alternatives and show great potential for practical device applications. However, the scope of such iSF materials remains rather limited, necessitating innovative molecular design strategies. Herein, we present how a side-chain ionization strategy leads to an iSF chromophore based on the azaquinodimethane (AQM) ring system. Systematic theoretical and spectroscopic analyses reveal that the direct attachment of electron-withdrawing ionic groups to the conjugated AQM core renders the originally fluorescent AQM nonemissive, leading to ionic AQM (iAQM) derivatives capable of ultrafast iSF to populate triplet-like species. Further fine-tuning of the iAQM skeleton imparts subtle intermolecular interactions that are indispensable for the efficient separation of triplet pairs following iSF in the aggregated state. Our findings offer unprecedented insights into molecular design and triplet exciton dynamics, laying the foundation for the discovery of rare molecular iSF materials.

Introduction

Singlet fission (SF) is an energy down-conversion process where organic semiconductors absorb one high-energy photon and generate one singlet which is then transformed into two triplet excitons.[1–3] Such an optically allowed multiexciton (ME) process could significantly alleviate thermalization losses of high-energy photons, thus holding great potential for improving the power conversion efficiency of solar cells.[4–6] In general, aside from fulfilling the singlet–triplet energetic requirement that $E(S_1) \approx 2E(T_1)$, conventional SF materials should be equipped with suitable intermolecular coupling interactions to achieve efficient ME generation, which requires an intricate control of molecular packing motifs in the solid state.[1–3] Perturbations in intermolecular interactions can significantly impact both the triplet formation rate and the yield of the SF process in high-concentration solutions and solid films. As a result, the active layer containing SF materials must be carefully deposited for fabricating high-performance devices, which restrict high-throughput processing methods and then we have to resort to primitive bilayer device architecture.[1–6] Recently, intramolecular SF (iSF) has emerged as a promising alternative mechanism to bypass these technical challenges as the SF process is an intrinsic molecular property. Thus, strong intermolecular coupling interactions and highly ordered crystalline domains are no longer necessary prerequisites, which allows for conventional solution-processing techniques and bulk heterojunction high-performance device architectures.[7–10] The iSF process has been observed in unimolecular acene dimers,[11–15] several conjugated polymers,[16–20] and a few small molecular systems.[21–28] Among these, small molecule iSF materials are particularly advantageous due to their unambiguous chemical structures, ease of synthesis and modification, excellent energy level tunability, and diverse processability. However, the scope of such iSF materials remains very limited compared to acene dimer and conjugated polymer iSF systems, which calls for rational approaches to modulating molecular excited state electronic structures for the development of efficient iSF small molecules.

[a]*Key Laboratory of Interface Science and Engineering in Advanced Materials, Ministry of Education, Taiyuan University of Technology, Taiyuan 030024, P. R. China. E-mail: wanglong@tyut.edu.cn*

[b]*The Molecular Foundry, Lawrence Berkeley National Laboratory, Berkeley, CA 94720, USA. E-mail: yliu@lbl.gov*

[c]*State Key Laboratory Breeding Base of Green Chemistry-Synthesis Technology, College of Chemical Engineering, Zhejiang University of Technology, Hangzhou 310014, P. R. China. E-mail: zhangts@zjut.edu.cn*

[d]*Beijing Key Laboratory for Optical Materials and Photonic Devices, Department of Chemistry, Capital Normal University, Beijing 100048, P. R. China. E-mail: hbfu@cnu.edu.cn*

† Electronic supplementary information (ESI) available. CCDC 2359138 and 2359139. For ESI and crystallographic data in CIF or other electronic format see DOI: https://doi.org/10.1039/d5sc01980j

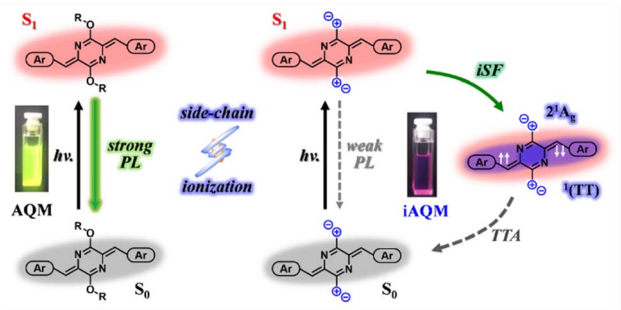

Scheme 1 Side-chain ionization enables an ultrafast iSF process in an AQM skeleton.

In this work, we present a series of unique iSF molecules based on the installation of ionic side groups on an azaquinodimethane (AQM) skeleton. Comprehensive theoretical and spectroscopic analyses, including concentration-dependent measurements, triplet sensitization experiments and multi-reference calculations, reveal that these ionic AQM (iAQM) molecules can undergo an ultrafast iSF process to populate triplet-like species (Scheme 1). By fine-tuning the conjugated structure of the iAQM core, we can engineer intermolecular interactions in solid aggregates to facilitate efficient triplet pair decoupling and the generation of free triplet excitons. Our molecular design is drastically different from the common oligomer approach to iSF-capable materials, which will stimulate future efforts in both fundamental structure–property relationship studies and practical applications.

Results and discussion

The quinoidal system and its steady-state characterization

AQM-core compounds feature distinctive optoelectronic properties and have been successfully applied in high-mobility semiconductor devices, polyelectrolytes and photothermal therapy.[29–33] Common neutral AQM derivatives usually exhibit intense fluorescent emission in solution (Scheme 1). However, upon side-chain ionization, the resulting ionic AQM (iAQM) derivatives become non-emissive, suggesting unusual excited state photophysics associated with their ionic quinoidal skeleton. We therefore compared two series of AQM-derived quinoidal systems containing varying numbers of thiophene donors, namely, the alkoxyl side-chain AQM-core series, **AQM1** and **AQM2**, and the ionic side-chain iAQM-core series, **iAQM1** and **iAQM2**. The single crystal structures of the two iAQM molecules are shown in Fig. 1b. **iAQM1** features a loose packing mode without obvious π–π interaction due to the steric effect imposed by the bulky triphenylphosphonium group. In contrast, **iAQM2** exhibits a slip-stacking motif with pronounced intermolecular π–π interactions between the elongated bisthiophene conjugated cores of adjacent molecules (π–π stacking distance: ~3.8 Å) despite the presence of bulky side groups. Steady state absorption and photoluminescence (PL) spectra were measured in dilute solutions of these AQM and iAQM derivatives (Fig. 1c). The two AQM molecules exhibited strong absorption peaks at around 445 and 531 nm and fluorescence

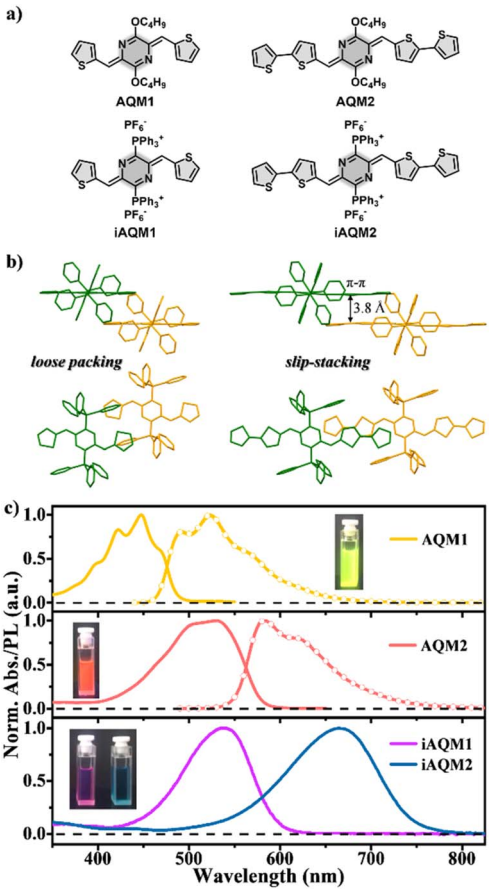

Fig. 1 (a) Chemical structures of the AQM and iAQM series. (b) Molecular packing motifs in single crystals of **iAQM1** and **iAQM2**. (c) Normalized absorption and PL spectra of **AQM1** (top, yellow solid and dashed lines, respectively) and **AQM2** (middle, red lines), and normalized absorption of **iAQM1** and **iAQM2** (bottom, purple and blue lines) in dilute solutions (DMF, 10^{-5} M). Insets show photographs of the solutions of AQMs and iAQMs under 365 nm light irradiation.

emission peaks at around 520 and 575 nm with PL quantum yields of 65% and 58%, respectively.[34] The two iAQM molecules exhibited strong absorption peaks at around 539 and 662 nm, respectively, but were nearly nonemissive, with extremely low PL efficiency (Φ_F < 0.01). The contrasting optoelectronic properties of AQM and iAQM derivatives suggest different relaxation pathways following initial optical excitation to their singlet (S_1) states, with more efficient non-radiative relaxation for the iAQM derivatives. Based on theoretical calculations, the singlet/triplet energies were estimated to be 2.34/0.89 and 1.82/0.72 eV for **iAQM1** and **iAQM2** molecules, respectively, which met the energetic requirement for SF (see Section 2 in the ESI,† for calculation details). These results suggest that the iSF process might be responsible for the rapid non-radiative excited state relaxation observed in the iAQM series compounds.

Excited state dynamics of neutral AQM derivatives

Transient absorption (TA) measurements were performed in order to reveal the excited state photophysics of these quinoidal molecules. The TA spectra of fluorescent AQM derivatives

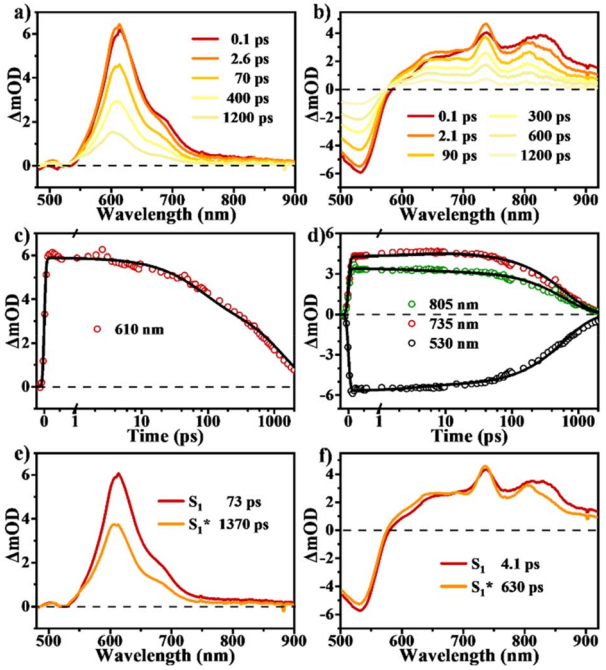

Fig. 2 Excited state dynamics of AQMs in dilute solutions. (a and b) TA spectra and (c and d) selected kinetic decay curves and (e and f) global analysis results for **AQM1** and **AQM2** molecules (excited at 450 nm).

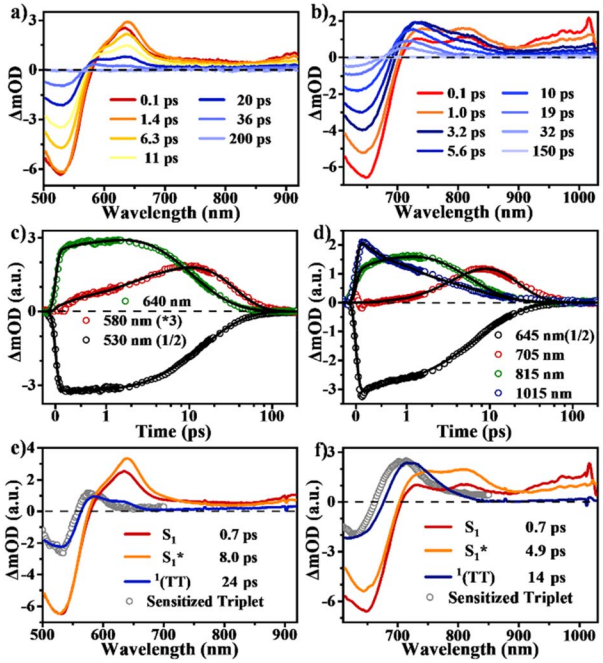

Fig. 3 Excited state dynamics of iAQMs in dilute DMF solutions. (a and b) TA spectra and (c and d) selected kinetic decay curves and (e and f) global analysis results for **iAQM1** and **iAQM2**, respectively (excited at 490/590 nm). The sensitized triplet curves are provided in (e and f) to help assign the triplet-like transient state species.

exhibit a simple spectral evolution indicative of the S_1 state deactivation process, namely, the fluorescence radiative transition (Fig. 2). Upon 450 nm photoexcitation of **AQM1** in its dilute solution, the corresponding TA spectra show a strong excited-state absorption (ESA) band at around 610 nm, which is assigned to the optically populated S_1 state (Fig. 2a and c). As the time delay increases, the ESA spectral line shapes display no obvious change from picosecond to nanosecond time scales. The TA spectra of **AQM2** display similar spectral evolution, showing a clear ground state bleaching (GSB) band at around 530 nm and a broad ESA band in the visible-to-NIR region (Fig. 2b and d). The TA data could be best fit to a sequential two-state kinetic model including an optically populated S_1 and a relaxed long-lived S_1^* state, with corresponding time constants of 73 and 1370 ps for **AQM1** and 4.1 and 630 ps for **AQM2**, respectively (Fig. 2e and f). These results are consistent with solution-based transient PL spectra (Fig. S2†), which indicate that simple singlet decay dominates the excited state deactivation process for these fluorescent AQM derivatives. In thin films, the AQM molecules are weakly emissive, attributed to a rapid SF process that outcompetes the radiative transition and dominates the excited state deactivation, as reported previously.[34]

ME dynamics of iAQM derivatives in solution

Subsequently, TA measurements were performed on **iAQM1** and **iAQM2** molecules to unveil the excited state photophysical processes associated with these side chain-ionized AQM derivatives (Fig. 3 and Table 1). In contrast to the long-lived transient behavior observed in the neutral AQM derivatives, the TA data from the dilute solutions of iAQMs display rapid spectral evolution and decay processes with short excited state lifetimes, in accordance with a different excited state deactivation process. It should be noted that the measurements were performed in dilute solutions, and the concentration-dependent experiments suggested that the observed dynamics were intramolecular rather than aggregate-induced or diffusion–collision-dominated (Fig. S5 and S6†). For **iAQM1**, upon photoexcitation at 490 nm, the resulting fs-TA spectra exhibit a clear GSB band at 530 nm and ESA bands peaked at 640 and 920 nm in the visible-to-NIR region, which are assigned to the optically populated S_1 state (Fig. 3a). The initial ESA band at around 920 nm starts to decay while the band at around 640 nm increases initially and then declines at longer time delays. Concurrent with the attenuation of these ESA bands, a new absorption band appears at around 580 nm and eventually

Table 1 Excited state globally fit kinetic rate constants and triplet yields derived from TA measurements of iAQMs in dilute DMF solution and thin films

Sample		$\tau[S_1/S_1^*]$/ps[a]	τ[TT]/ps[a]	$\tau[T_1]$/μs[b]
Sol.	**iAQM1**	0.7 ± 0.2/8.0 ± 1.2	24 ± 4	—
	iAQM2	0.7 ± 0.2/4.9 ± 0.7	14 ± 3	—
Films	**iAQM1**	4.3 ± 0.8	62 ± 11	—
	iAQM2	2.3 ± 0.4	67 ± 10	0.25 ± 0.02 10.3 ± 1.0

[a] The kinetic rate constants obtained from global analysis based on the two-/three-state model for TA data. [b] Triplet lifetimes obtained from ns-TA measurements for **iAQM2** film.

decays to the baseline along with the GSB signals (Fig. 3a and c). The TA spectra of **iAQM2** exhibit a similar yet more distinct spectral evolution (Fig. 3b and d). Photoexcitation at 590 nm populates the GSB signals at around 645 nm and the ESA bands of the S_1 state at around 900–1000 nm, which gradually evolve into ESA bands at around 700–800 nm. As these bands decline, a new absorption band appears at around ~700 nm and eventually decays to the baseline along with the GSB signals, mirroring the behavior observed in the spectra of **iAQM1**. No long-lived signals are detected in the TA spectra from these solution measurements.

The TA data were best fit to a sequential three-state kinetic model with three distinct time constants of 0.7, 8.0, and 24 ps for **iAQM1**, and 0.7, 4.9, and 14 ps for **iAQM2**, respectively, which depicted the dynamic evolution of various transient species (Fig. 3e and f). The species-associated spectra were then compared with the absorption signatures of the sensitized triplet state obtained from triplet sensitization experiments (for details see Section 4.4 in the ESI, Fig. S8 and S9†). The initial species is in the optically populated S_1 state. The spectrum of the intermediate species resembles that of the initial S_1 species, which is assigned to the relaxed singlet (S_1^*) state. The spectrum of the long-lived species is nearly identical to the sensitized triplet curve, suggesting that it is a transient species with distinct triplet character (Fig. 3e and f). Due to the short lifetimes of ~20 ps, which are six orders of magnitude lower than that of free triplets, we assign this species to the SF-produced, strongly coupled triplet pair state, namely ^{1}(TT). Considering the ultrafast population rate and short lifetime of the triplet-like species, we exclude the intersystem crossing pathway to free triplets. Moreover, we synthesized a reference compound, **iAQM3**, an ionic iAQM derivative bearing pyridinium side groups instead of phosphonium groups (for details see Section 4.5 in the ESI†), to probe the heavy-atom effect of phosphorus. The TA measurements of **iAQM3** showed almost identical excited state photophysical processes, featuring ultrafast triplet pair formation (Fig. S10†), suggesting the absence of the heavy-atom effect. Although the exciton dynamics exhibits small solvent polarity dependence (Fig. S11†), we exclude the possibility of intramolecular charge transfer (CT) species considering the distinctive ESA signature of such polaron species in the NIR region, similar to that described in our previous work.[19] Using the molar absorption coefficient method, the triplet generation yields in the triplet pairs of **iAQM1** and **iAQM2** molecules in dilute solution were estimated to be 140 ± 30% and 170 ± 30%, respectively (for details see Section 4.7 in the ESI†). Returning to the ground state *via* geminate recombination on the ionic skeleton is deemed responsible for the short lifetime of the triplet pairs. These results clearly confirm that an ultrafast and quantitative iSF process dominates the excited state deactivation, leading to fluorescence quenching in the ionized AQM derivatives.

Theoretical calculations for capturing the ME state

To capture the intramolecular ME state, we then investigated the excited-state electronic structure of the AQM and iAQM systems based on multi-reference theoretical calculations (for calculation details see Section 5 in the ESI†).[35,36] To streamline the computational process, we simplified the model molecules by omitting lengthy alkyl chains and benzene rings. Throughout these calculations, a C_i symmetry constraint for the molecular structures and orbitals was used. Geometry optimization for these structures was performed at the SA4-CAS(14,14)/ANO-RCC-VDZP level of theory.[37] Subsequently, the reported energy values were derived using the XDW-CASPT2 method.[36] On the basis of the optimized ground-state (S_0, 1^1A_g) structure, we explored the electronic structures of the relevant excited states, *i.e.*, $1^1A_g(S_0)$, $2^1A_g(S_1)$, $1^1A_u(S_2)$, and $1^3A_u(T_1)$ states (Fig. 4 and Table 2). The results show that the neutral AQM and ionized iAQM molecules have similar electronic structures with the major excited states. The symmetry-allowed H → L singly excited transition leads to the optically bright $1^1A_u(S_1)$ state with the electronic configuration (A_g2222u00/A_u22d0000). A dark state (2^1A_g) is found close to the bright state and has the double excitation character that involves simultaneous promotion of two electrons from occupied to unoccupied orbitals, specifically the H → L transition with an electronic configuration of (A_g2222200/A_u2200000), clearly indicating its distinct ME nature. The difference between the neutral and ionized systems appeared in the relative energy level arrangements of the involved excited states. In the neutral AQM system, the dark ME(2^1A_g) state was almost energy-degenerate with the bright $S_1(1^1A_u)$ state, while in the ionized iAQM system, the ME(2^1A_g) was separated from the bright $S_1(1^1A_u)$ state. Therefore, we suppose that the energy-degeneracy arrangements render the interconversion process between the dark ME(2^1A_g) and bright $S_1(1^1A_u)$ states very rapid resulting in a bright state-dominated fluorescent molecular system, given the spin-allowed nature of the $S_1(1^1A_u) \rightarrow S_0(1^1A_g)$ transition. By contrast, the separated energy level arrangements in the ionized iAQM molecule lead to a dark ME state-dominated iSF molecular system. In the minimum energy regions, the $1^1A_u(S_1)$, 2^1A_g ME and $1^3A_u(T_1)$ states are at 2.02, 2.23, and 1.02 eV for the iAQM molecule, respectively (Table 2). Thus, the SF energetic requirements are fulfilled from both the bright 1^1A_u and 2^1A_g ME dark states, and the proximity of the two states in energy causes the conversion from the bright 1^1A_u to the 2^1A_g ME dark state, namely the iSF process, to occur at ultrafast rates as evidenced by the above experimental results. The results further confirm that an ultrafast iSF process mediated by a key dark ME state dominates

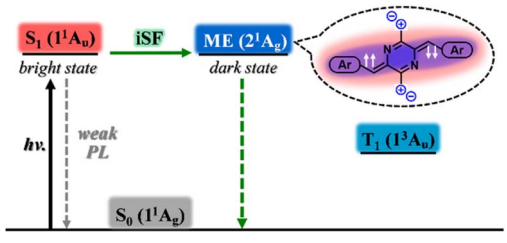

Fig. 4 Key dark ME state dominates the excited state deactivation of iAQMs.

Table 2 Excited state energy diagram of the AQM and iAQM systems

	State	Excited energy[a]/eV	Configuration A_g/A_u[b]	Oscillator strength
AQM	$S_0(1^1A_g)$-MIN	—	2222000/2220000	—
	$S_1(1^1A_u)$-FC/MIN (bright)	3.30/2.48	2222u00/22d0000	1.22/1.20
	$ME(2^1A_g)$-FC/MIN (dark)	2.91/2.54	2222200/2200000	0.0/0.0
	$T_1(1^3A_u)$-MIN	1.23	2222u00/22u0000	—
iAQM	$S_0(1^1A_g)$-MIN	—	2222000/2220000	—
	$S_1(1^1A_u)$-FC/MIN (bright)	2.25/2.02	2222u00/22d0000	1.29/1.28
	$ME(2^1A_g)$-FC/MIN (dark)	2.45/2.23	2222200/2200000	0.0/0.0
	$T_1(1^3A_u)$-MIN	1.02	2222u00/22u0000	—

[a] Vertical/minimum excited energy. [b] Electronic configuration describes the occupation of the 14 electrons in the 14 molecular orbitals, in which 2: occupied by two electrons, u: a single electron with "up" spin, d: a single electron with "down" spin, and 0: empty. 14 molecular orbitals fall into two irreducible representations, namely A_g and A_u.

the excited state deactivation of the ionized AQM derivatives (Fig. 4).

Aggregated state ME dynamics of iAQM derivatives

We subsequently investigated the spuncast thin films of iAQMs to further decipher the iSF mechanism and corresponding ME dynamics. In steady-state absorption spectra, the iAQM thin films show varying degrees of spectral broadening and red shift (Fig. 5a) due to their contrasting molecular packing motifs in the aggregated state (Fig. 1b). Compared to its solution state absorption, the **iAQM1** film features an absorption peak at around 552 nm with slight spectral broadening, consistent with the lack of strong intermolecular interactions due to loose packing in the solid state. In contrast, the **iAQM2** film shows an absorption peak at around 705 nm with an obvious red shift compared to its solution spectrum, which is correlated with considerable aggregation facilitated by the slip-stacking π–π interactions. Both thin films of **iAQM1** and **iAQM2** are only weakly fluorescent. Powder X-ray diffraction (PXRD) patterns of the thin films indicate that **iAQM1** is more amorphous than **iAQM2**, as evidenced by the much greater fullwidth at half maximum (FWHM) of the diffraction peaks than those of **iAQM2** (Fig. 5b). These distinct molecular packing motifs correlate with the essential photophysical characteristics of the iAQM molecules in solid aggregates.

TA measurements of the **iAQM1** film reveal similar spectral line shapes and evolution trends as those observed in its dilute solution, indicating that the excited state behavior is intrinsic to individual molecules due to loose molecular packing in both solution and thin films (Fig. 6a, c and e). The TA results are well interpreted using a similar sequential two-state kinetic model with corresponding time constants of 4.3 and 63 ps (Fig. 6e). These results demonstrate that loose-packing **iAQM1** molecules undergo a rapid iSF process at a rate constant of $(4.3\ \text{ps})^{-1}$. The slightly longer lifetime of the SF-produced triplet pairs in the solid aggregates compared to their solution counterparts can be ascribed to exciton stabilization in the solid state. In contrast, the **iAQM2** film exhibits marked spectral differences compared to its dilute solution, including (i) significant overlap of the red-shifted GSB signals with the ESA bands and (ii) the appearance of long-lived transient species with a lifetime over several

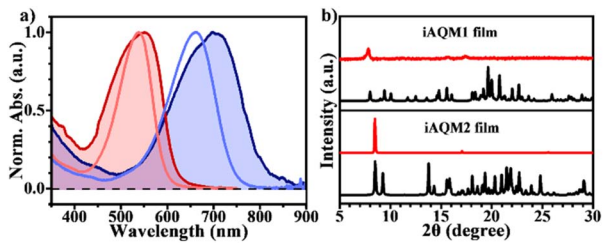

Fig. 5 Aggregated state characterization. (a) Normalized absorption spectra of **iAQM1** (red lines) and **iAQM2** (blue lines) molecules in dilute solutions (light colored lines, 10^{-5} M in DMF) and thin films (dark lines filled with color). (b) PXRD diffractograms (red) and simulated powder patterns (black) of **iAQM1** and **iAQM2** thin films.

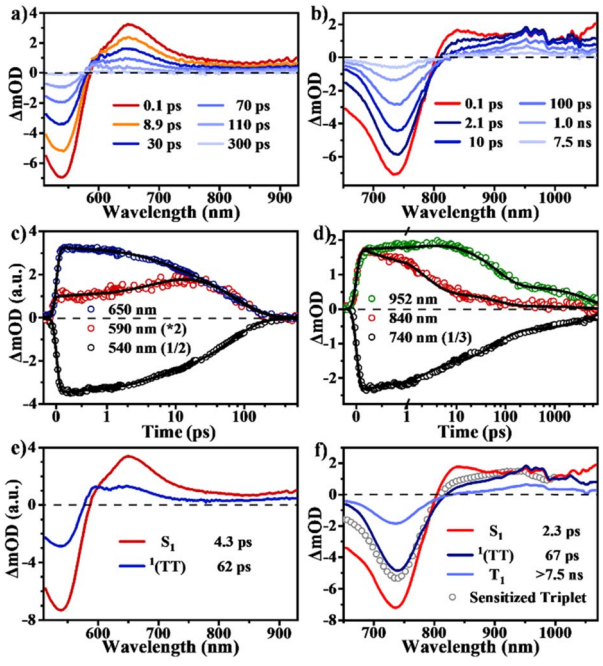

Fig. 6 Excited state dynamics of iAQMs in thin films. (a and b) TA spectra and (c and d) selected kinetic decay curves and (e and f) global analysis results for **iAQM1** and **iAQM2** films (excited at 490/640 nm). The sensitized triplet curve is provided in (f) to help assign the triplet-like transient state species.

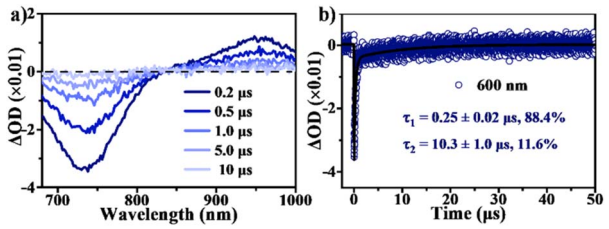

Fig. 7 Triplet state decay dynamics in **iAQM2** thin films. (a) ns-TA spectra and (b) selected kinetic decay curves for **iAQM2** films (excited at 532 nm).

nanoseconds (Fig. 6b, d and f). Beyond these spectral differences, the molecules still undergo an ultrafast iSF process and subsequent dynamic evolution of different ME states, as further evidenced by triplet sensitization experiments in the solid film.

Specifically, photoexcitation at 640 nm results in TA spectra composed of a strong GSB signal at around 740 nm and broad ESA bands peaked at 840, 950, and 1070 nm (Fig. 6b). Despite serious overlap, the spectral evolution at the initial stage resembles that in dilute solution, where the initial ESA bands at around ~800 and over 1000 nm are rapidly attenuated, while a new transient species arises at around 700 nm, resulting in line shape changes and an intensity decrease in the GSB signals. The newly formed ESA bands are long-lived and can persist beyond the 7.5 ns detection time window of our TA setup. The TA data are best fit to a sequential three-state kinetic model with three time constants of 2.3 ps, 67 ps, and >7.5 ns (Fig. 6f). The first transient species is assigned to the optically populated S_1 state. The species-associated spectra of the intermediate and final species overlap well with the sensitized triplet curves (Fig. 6f, for triplet sensitization experiment details see Section 6.4 in the ESI, Fig. S19–S22†), suggesting that they are transient species with distinct triplet character. Given the similarity in spectral evolution between the solution and thin film results and based on the global analysis results of the film, we assign the two transient species to the triplet pair and free triplet states, namely, ^{1}(TT) and T_1 states, respectively. Despite this, we cannot completely exclude the coherent mechanism of ME generation based on the current experimental data, which need to be verified using further spectroscopic evidence.[38] In order to track the exciton dynamics of the dissociated free triplets, we performed nanosecond TA (ns-TA) measurements of **iAQM2** films. The results show that these free triplets exhibit biexponential decay kinetics with lifetimes of $\tau_1 = 0.25 \pm 0.02$ μs (88.4%) and $\tau_2 = 10.3 \pm 1.0$ μs (11.6%) (Fig. 7). We attribute the two different decay components to triplets undergoing prompt triplet–triplet annihilation and those diffusing away from one another until annihilation, respectively. Using the previously reported singlet depletion method,[39] a triplet yield for **iAQM2** film was estimated to be 140 ± 30% (for details see Section 6.4 in the ESI†). In the strongly coupled **iAQM2** film, the excited state molecules undergo an ultrafast iSF process to populate the ^{1}(TT) state at a rate of 2.3 ps. Subsequently, the populated ^{1}(TT) state decouples and separates into two individual triplets at a rate of 67 ps. Finally, the free triplet state persists for several nanoseconds before returning back to the ground state.

Discussion

Based on the systematic structural analysis and photophysical measurements, we conclude that an ultrafast iSF process outcompetes radiative transition channels and dominates the excited state deactivation of the iAQM system. The side-chain ionization renders the originally fluorescent neutral AQM molecules nonluminous because the resultant iAQM molecules undergo an ultrafast iSF process to populate triplet-like species. The overall iSF processes of the iAQM system are summarized in the schematic diagram (Scheme 2). In dilute solutions where the molecules are isolated, the optically populated S_1 exciton relaxes to the stabilized S_1^* state and then undergoes an ultrafast iSF process to generate intramolecular triplet pair species located on different sides of the iAQM skeleton. These triplet pair species then return to the ground state *via* geminate recombination due to strong coupling character, which is responsible for their short lifetimes. In solid aggregates, iAQM molecules also undergo the iSF process and form triplet pair species. In the film of **iAQM1** where molecules are loosely packed similar to the dilute solution state, the triplet pairs are somewhat stabilized but not fully dissociated, resulting in a slightly longer exciton lifetime. Consequently, these triplet pairs suffer from rapid geminate recombination, as observed in the solution state. In contrast, in the strongly coupled film of **iAQM2**, the system not only undergoes rapid iSF to populate ME

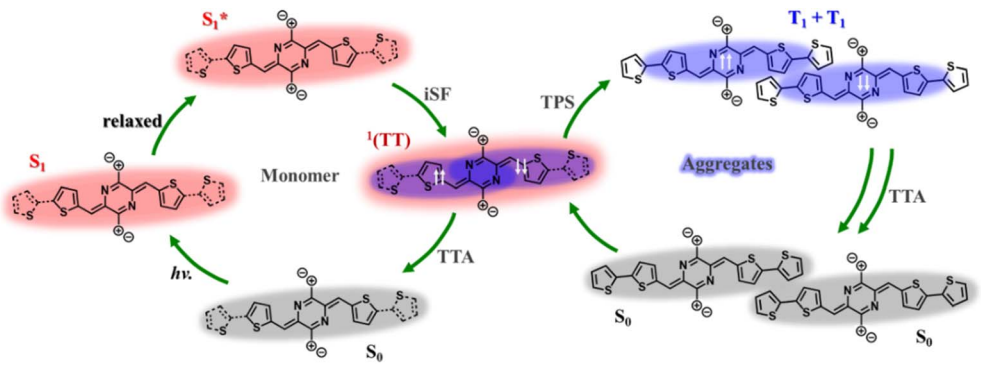

Scheme 2 Schematic diagram summarizing the iSF processes in the iAQM system.

species, but also achieves efficient triplet pair separation (TPS) to generate long-lived free triplet excitons. Favorable intermolecular interactions in solid aggregates allow the iSF-produced ME species to further diffuse to suitable sites and dissociate into individual triplets. It should be noted that the π–π interaction distance of ~3.8 Å observed in **iAQM2** is significantly larger than that reported in other intermolecular SF systems, which is usually ~3.4 Å.[40–43] This difference supports that iSF materials have less stringent requirements for intermolecular interactions to achieve efficient ME generation processes.[7–10]

Conclusions

A series of iSF molecules based on the distinctive ionic AQM chromophore has been successfully developed. Through a combination of structural analysis, theoretical calculation and transient absorption spectroscopy, we have validated that side-chain ionization enables efficient non-radiative pathways, rendering the originally fluorescent AQM skeleton nonluminous. In dilute solutions, the iAQM molecules undergo ultrafast iSF processes to populate triplet-like species, while in solid aggregates, favorable intermolecular interactions facilitate the efficient decoupling of triplet pairs into free triplet excitons. Our findings introduce innovative chromophores with untapped iSF capabilities, offering rational design principles that could inform the discovery of a broader range of molecular iSF materials with intricate multiexciton dynamics.

Data availability

The data supporting this article have been included as part of the Supplementary Information. Crystallographic data for iAQM1 and iAQM2 has been deposited at the CCDC under 2359138 and 2359139 can be obtained from **www.ccdc.cam.ac.uk/data_request/cif**.

Author contributions

L. W., Y. L. and H. B. F. conceptualized and conceived the project. Z. X. W. prepared samples and conducted the photophysical characterization and performed the data analysis, which were supervised by L. W. and H. B. F. C. L. A. and Y. L. provided the compounds. T. S.-Z. performed the theoretical simulations. L. W. and Y. L. wrote the manuscript and all the authors participated in the data analysis and discussions.

Conflicts of interest

There are no conflicts to declare.

Acknowledgements

This work was supported by the National Natural Science Foundation of China (No. 22479107 and 22005210) and by the Fundamental Research Program of Shanxi Province (No. 202203021224004 and 20210302124469). Part of the work was carried out as a user project at the Molecular Foundry, a user facility supported by the Office of Science, Office of Basic Energy Sciences, of the U.S. Department of Energy under Contract No. DE-AC02-05CH11231.

Notes and references

1 M. B. Smith and J. Michl, *Chem. Rev.*, 2010, **110**, 6891–6936.
2 A. Rao and R. H. Friend, *Nat. Rev. Mater.*, 2017, **2**, 17063.
3 T. Ullrich, D. Munz and D. M. Guldi, *Chem. Soc. Rev.*, 2021, **50**, 3485–3518.
4 W. Shockley and H. J. Queisser, *J. Appl. Phys.*, 1961, **32**, 510–519.
5 M. C. Hanna and A. J. Nozik, *J. Appl. Phys.*, 2006, **100**, 074510.
6 D. N. Congreve, J. Y. Lee, N. J. Thompson, E. Hontz, S. R. Yost, P. D. Reusswig, M. E. Bahlke, S. Reineke, T. Van Voorhis and M. A. Baldo, *Science*, 2013, **340**, 334–337.
7 J. L. Xia, S. N. Sanders, W. Cheng, J. Z. Low, J. P. Liu, L. M. Campos and T. L. Sun, *Adv. Mater.*, 2017, **29**, 1601652.
8 H. Kim and P. M. Zimmerman, *Phys. Chem. Chem. Phys.*, 2018, **20**, 30083–30094.
9 K. Miyata, F. S. Conrad-Burton, F. L. Geyer and X. Y. Zhu, *Chem. Rev.*, 2019, **119**, 4261–4292.
10 T. Wang, H. Liu, X. Wang, L. Tang, J. Zhou, X. Song, L. Lv, W. Chen, Y. Chen and X. Li, *J. Mater. Chem. A*, 2023, **11**, 8515–8539.
11 A. M. Müller, Y. S. Avlasevich, W. W. Schoeller, K. Müllen and C. J. Bardeen, *J. Am. Chem. Soc.*, 2007, **129**, 14240–14250.
12 J. Zirzlmeier, D. Lehnherr, B. C. Pedro, T. C. Erin, R. Casillas, S. B. Bettina, M. Thoss, R. T. Rik and M. G. Dirk, *Proc. Natl. Acad. Sci. U. S. A.*, 2015, **112**, 5325–5330.
13 E. A. Margulies, C. E. Miller, Y. L. Wu, L. Ma, G. C. Schatz, R. M. Young and M. R. Wasielewski, *Nat. Chem.*, 2016, **8**, 1120–1125.
14 Z. Wang, H. Liu, X. Xie, C. Zhang, R. Wang, L. Chen, Y. Xu, H. Ma, W. Fang, Y. Yao, H. Sang, X. Wang, X. Li and M. Xiao, *Nat. Chem.*, 2021, **13**, 559–567.
15 G. He, L. M. Yablon, K. R. Parenti, K. J. Fallon, L. M. Campos and M. Y. Sfeir, *J. Am. Chem. Soc.*, 2022, **144**, 3269–3278.
16 M. Wohlgenannt, W. Graupner, R. Österbacka, G. Leising, D. Comoretto and Z. V. Vardeny, *Synth. Met.*, 1999, **101**, 267–268.
17 E. Busby, J. L. Xia, Q. Wu, J. Z. Low, R. Song, J. R. Miller, X. Y. Zhu, L. M. Campos and M. Y. Sfeir, *Nat. Mater.*, 2015, **14**, 426–433.
18 J. H. Hu, K. Xu, L. Shen, Q. Wu, G. Y. He, J. Y. Wang, J. Pei, J. L. Xia and M. Y. Sfeir, *Nat. Commun.*, 2018, **9**, 2999.
19 L. Wang, X. Liu, X. Shi, C. L. Anderson, L. M. Klivansky, Y. Liu, Y. Wu, J. Chen, J. Yao and H. Fu, *J. Am. Chem. Soc.*, 2020, **142**, 17892–17896.
20 X. Shi, Y. Geng, Z. Wang, E. Zhou, H. Fu and L. Wang, *Adv. Funct. Mater.*, 2025, 2420771.
21 M. T. Trinh, Y. Zhong, Q. S. Chen, T. Schiros, S. Jockusch, M. Y. Sfeir, M. Steigerwald, C. Nuckolls and X. Y. Zhu, *J. Phys. Chem. C*, 2015, **119**, 1312–1319.
22 O. Varnavski, N. Abeyasinghe, J. Arago, J. J. Serrano-Perez, E. Orti, J. T. L. Navarrete, K. Takimiya, D. Casanova,

J. Casado and T. Goodson, *J. Phys. Chem. Lett.*, 2015, **6**, 1375–1384.
23 Y. S. Wu, Y. C. Wang, J. W. Chen, G. X. Zhang, J. N. Yao, D. Q. Zhang and H. B. Fu, *Angew. Chem., Int. Ed.*, 2017, **56**, 9400–9404.
24 L. Wang, S. Bai, Y. Wu, Y. Liu, J. Yao and H. Fu, *Angew. Chem., Int. Ed.*, 2020, **59**, 2003–2007.
25 L. Wang, T.-S. Zhang, L. Fu, S. Xie, Y. Wu, G. Cui, W.-H. Fang, J. Yao and H. Fu, *J. Am. Chem. Soc.*, 2021, **143**, 5691–5697.
26 L. Mencaroni, B. Carlotti, F. Elisei, A. Marrocchi and A. Spalletti, *Chem. Sci.*, 2022, **13**, 2071–2078.
27 L. Wang, L. Lin, T.-S. Zhang, S. Guo, Z. Liu, M. Zhang, S. Wang, G. Cui, W.-H. Fang, J. Zhu, H. Fu and J. Yao, *CCS Chem.*, 2023, **5**, 2264–2276.
28 S. Wang, X.-Y. Liu, M. Zhang, L. Wang, G. Cui, H. Fu and J. Yao, *CCS Chem.*, 2024, **6**, 2142–2149.
29 X. Liu, B. He, C. L. Anderson, J. Kang, T. Chen, J. Chen, S. Feng, L. Zhang, M. A. Kolaczkowski, S. J. Teat, M. A. Brady, C. Zhu, L.-W. Wang, J. Chen and Y. Liu, *J. Am. Chem. Soc.*, 2017, **139**, 8355–8363.
30 C. L. Anderson, N. Dai, S. J. Teat, B. He, S. Wang and Y. Liu, *Angew. Chem., Int. Ed.*, 2019, **58**, 17978–17985.
31 H. Liang, C. Liu, Z. Zhang, X. Liu, Q. Zhou, G. Zheng, X. Gong, L. Xie, C. Yang, L. Zhang, B. He, J. Chen and Y. Liu, *Adv. Funct. Mater.*, 2022, **32**, 2201903.
32 X. Liu, C. L. Anderson and Y. Liu, *Acc. Chem. Res.*, 2023, **56**, 1669–1682.
33 Z. Zhao, S. Wang, X. Shi, H. Fu and L. Wang, *Chem. Sci.*, 2025, **16**, 5565–5572.
34 L. Wang, X. Shi, S. Feng, W. Liang, H. Fu and J. Yao, *CCS Chem.*, 2022, **4**, 2748–2756.
35 F. Aquilante, J. Autschbach, A. Baiardi, S. Battaglia, V. A. Borin, L. F. Chibotaru, I. Conti, L. De Vico, M. Delcey, I. F. Galván, N. Ferré, L. Freitag, M. Garavelli, X. Gong, S. Knecht, E. D. Larsson, R. Lindh, M. Lundberg, P. Å. Malmqvist, A. Nenov, J. Norell, M. Odelius, M. Olivucci, T. B. Pedersen, L. Pedraza-González, Q. M. Phung, K. Pierloot, M. Reiher, I. Schapiro, J. Segarra-Martí, F. Segatta, L. Seijo, S. Sen, D.-C. Sergentu, C. J. Stein, L. Ungur, M. Vacher, A. Valentini and V. Veryazov, *J. Chem. Phys.*, 2020, **152**, 214117.
36 S. Battaglia and R. Lindh, *J. Chem. Phys.*, 2021, **154**, 034102.
37 B. O. Roos, R. Lindh, P.-Å. Malmqvist, V. Veryazov and P.-O. Widmark, *J. Phys. Chem. A*, 2004, **108**, 2851–2858.
38 W.-L. Chan, T. C. Berkelbach, M. R. Provorse, N. R. Monahan, J. R. Tritsch, M. S. Hybertsen, D. R. Reichman, J. Gao and X. Y. Zhu, *Acc. Chem. Res.*, 2013, **46**, 1321–1329.
39 S. W. Eaton, S. A. Miller, E. A. Margulies, L. E. Shoer, R. D. Schaller and M. R. Wasielewski, *J. Phys. Chem. A*, 2015, **119**, 4151–4161.
40 L. Wang, L. Lin, J. Yang, Y. Wu, H. Wang, J. Zhu, J. Yao and H. Fu, *J. Am. Chem. Soc.*, 2020, **142**, 10235–10239.
41 L. Wang, W. Cai, J. Sun, Y. Wu, B. Zhang, X. Tian, S. Guo, W. Liang, H. Fu and J. Yao, *J. Phys. Chem. Lett.*, 2021, **12**, 12276–12282.
42 L. Wang, W. Jiang, S. Guo, S. Wang, M. Zhang, Z. Liu, G. Wang, Y. Miao, L. Yan, J.-Y. Shao, Y.-W. Zhong, Z. Liu, D. Zhang, H. Fu and J. Yao, *Chem. Sci.*, 2022, **13**, 13907–13913.
43 Z. Liu, L. Wang, Q. Deng, J. Zhu, J. Sun, H. Wang, H. Fu and J. Yao, *ACS Mater. Lett.*, 2023, **5**, 3010–3016.